Chinese Chemical Letters 35 (2024) 108477

Contents lists available at ScienceDirect

Chinese Chemical Letters

journal homepage: www.elsevier.com/locate/cclet

# Anion-induced differential assembly and structural transformation of supramolecular coordination cages

Shao-Ping Zheng[a], Yao-Wei Xu[a], Pei-Yang Su[a,b], Chen-Hui Liu[a], Yin-Hui Huang[a], Yu-Lin Lu[a], Zhang-Wen Wei[a], Zhiwei Jiao[a], Hai-Sen Xu[a,*], Cheng-Yong Su[a,c,*]

[a] *MOE Laboratory of Bioinorganic and Synthetic Chemistry, Lehn Institute of Functional Materials, School of Chemistry, Sun Yat-sen University, Guangzhou 510006, China*
[b] *Institute of Environmental Research at Greater Bay Area, Guangzhou University, Guangzhou 510006, China*
[c] *State Key Laboratory of Organometallic Chemistry, Shanghai Institute of Organic Chemistry, Chinese Academy of Sciences, Shanghai 200032, China*

ARTICLE INFO

*Article history:*
Received 22 February 2023
Revised 11 April 2023
Accepted 18 April 2023
Available online 19 April 2023

*Keywords:*
Supramolecular coordination cage
Dynamic host-anion interactions
Structural transformation
Anion receptor
Guest inclusion

ABSTRACT

The intimate host-anion interactions will regulate thermodynamics and kinetics in the self-assembly of cationic cages mimicking biological counterparts. Herein, we report construction and transformation of three Pd(II)-based metal-organic cages (MOCs) depending on different anions. Stoichiometric conversions of the lantern-shaped **MOC-34** into either octahedral **MOC-35** or tricapped trigonal prism **MOC-36** are induced by $BF_4^-$ or $NO_3^-$, respectively. **MOC-36** is kinetically favored and can undergo quantitative conversion to the thermodynamically preferred **MOC-35** upon heating, accelerated by excess $BF_4^-$ to motivate dissociative dynamics of Pd-vertices and lower activation barrier of cage transformation. The guest encapsulation behaviors of **MOC-35** and **MOC-36** have also been tested. These results manifest a significance of host-anion dynamics beyond complementary anion template, shedding light on the understanding of intricate anion recognition in nature.



The generation of exquisite and complex architectures from relatively simple molecular precursors through noncovalent interaction is ubiquitous in nature [1]. Over the past decades, the self-assembly of metal-organic cages (MOCs) offers a controllable platform at the molecular level to mimic biological counterparts such as protein receptors and enzymes [2–4], in which the spatial arrangement and directionality of the components are well-defined owing to a thermodynamic control of the error correction of the reversible bonds [5,6]. However, different self-assembling progresses often equilibrate to present a distribution in delicate balance, which is tunable depending on external stimuli [7–9], *e.g.*, guest [10,11], concentration [12,13], solvent [14–16], *etc.* Substantial effort has been devoted to illuminating the principles governing the self-assembly processes from the same building blocks [17–19]; nevertheless, precise prediction in many cases still remains an elusive challenge [5,20,21].

Benefited from electrostatic and hydrogen-bonding interactions, anions have been widely employed in self-organization [22], recognition [23–25] and transformation [26,27]. For instance, anionic templates with shape complementarity and ideal packing coefficient were added to the system to drive the formation of inaccessible complicated supramolecular architectures [15,28]. In addition to the mutual matching host–guest complexation [29], dynamic associations of the counterions around a cationic host with large holes opening to the exterior are common phenomena in solution, but are neglected in most cases. Such anion binding may impose elaborate perturbation on the constitutional dynamic libraries (CDLs) [7,8] in solution, thus resulting in various thermodynamic and/or kinetic binding events to lead to structural regulation [30–32], reminiscent of the induced-fit mechanism observed in biological receptors [33]. Moreover, it is of interest to explore how the supramolecular isomerism in coordination self-assembly can be controlled by anions in different structural orders, considering that it has been extensively investigated in polymeric and cyclic systems [20,34–36], but less studied in cage system, compared other external stimuli such as guests, concentration, solvent, pH, and light [12,17,26,28,37–39].

Here, we report differential assembly and transformation of three MOCs, *i.e.*, one $Pd_2L_4$ (**MOC-34**) cage and two $(Pd_3L_4)_{2\text{-}3}$

* Corresponding authors at: MOE Laboratory of Bioinorganic and Synthetic Chemistry, Lehn Institute of Functional Materials, School of Chemistry, Sun Yat-sen University, Guangzhou 510006, China.
*E-mail addresses:* xuhs@mail.sysu.edu.cn (H.-S. Xu), cesscy@mail.sysu.edu.cn (C.-Y. Su).

https://doi.org/10.1016/j.cclet.2023.108477
1001-8417/

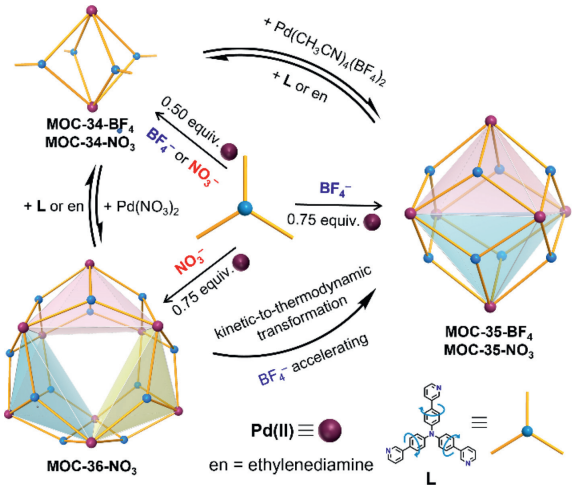


**Scheme 1.** Anion-induced assembly and conversion. Note: **MOC-36** only exists with $NO_3^-$ as counter anion, and **MOC-35-NO$_3$** only form from an **MOC-36-to-MOC-35** cage conversion.

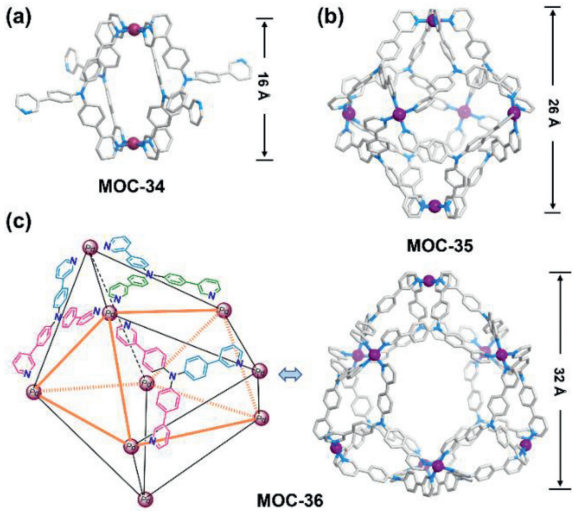


**Fig. 1.** Single-crystal structures of **MOC-34** and **MOC-35**, and the modeled structure of **MOC-36**. Molecular drawing of **MOC-36** shows three inequivalent pyridyl arms (in different color) binding to different Pd-vertices, *i.e.*, binding to the capping Pd-vertices, binding to the side edge Pd-vertices, and binding to the base edge Pd-vertices. Anions and hydrogen atoms are omitted for clarity.

supramolecular isomeric cages (**MOC-35** and **MOC-36**), induced by $BF_4^-$ or $NO_3^-$ anions (Scheme 1). Based on the experiments and theoretical calculations, we find that the host-anion dynamic interactions play a significant role beyond anion template effect in the regulation of thermodynamics and kinetics in cage transformation. The anion-induced interconversion between the smaller $Pd_6L_8$ and larger $Pd_9L_{12}$ can tune the confined environment, thus generating distinct host–guest interactions for guest inclusion.

A tridentate torsional compound, tris(4-(pyridin-3-yl)phenyl) amine (L), was synthesized as the organic ligand. Owing to the $C_3$-symmetric propeller shape and the free twist of $N_{Py}$-sites, its assembly with the four-coordination $Pd^{2+}$ is expected to form different cage structures with variable composition (Scheme 1 and Fig. 1). A lantern-shaped cage **MOC-34** was obtained by mixing L and 0.5 equiv. $Pd(NO_3)_2$ or $[Pd(CH_3CN)_4](BF_4)_2$ in DMSO at room temperature for 2 h. $^1$H NMR spectrum presents proton signals corresponding to a $Pd_2L_4$ cage structure containing the degraded $C_2$-symmetric ligand, which has been fully characterized by $^{13}$C, $^1$H-$^1$H COSY, $^1$H-$^{13}$C HSQC, $^1$H DOSY NMR and ESI-HR-MS (electrospray ionization–high-resolution mass) spectral measurements (Figs. S1–S7 in Supporting information). The single-crystal diffraction analysis (Fig. 1a and Table S1 in Supporting information) confirms that **MOC-34** is composed of four bidentate ligands and two $Pd^{2+}$ cations, in which only two $N_{Py}$-sites of each ligand participate in coordination with the Pd-centers, leaving one pyridyl arm uncoordinated.

Since the tridentate ligands in **MOC-34** show unsaturated coordination, we expect that even larger cage structures could be self-assembled by increasing the feeding ratio of metal/ligand (Pd/L > 1/2). Indeed, a clear solution was obtained by mixing L and 0.75 equiv. $[Pd(CH_3CN)_4](BF_4)_2$ (Pd/L = 3/4) in DMSO at 353 K for 4 h, and the $^1$H NMR spectrum displayed an uniformed proton signal pattern (Fig. S1) experiencing apparent downfield shift when compared with the free ligand, indicating that the three pyridyl arms are $C_3$-symmetrically coordinated with Pd-centers to constitute a $Pd_6L_8$ type cage (**MOC-35**, Scheme 1 and Fig. 1b). The formation of $Pd_6L_8$ cage structure has been further confirmed by the detailed NMR and ESI-HR-MS spectral measurements (Figs. S8–S13 in Supporting information), in which the single diffusion band ($\log D = -10.1$) in $^1$H DOSY spectrum suggests a dynamic radius of 13.8 Å for the cage (Fig. S12), and the neat series of successively charged $[(Pd_6L_8)^{12+}+nBF_4]^{(12-n)+}$ species indicate the presence of the sole **MOC-35** product in solution (Fig. S13). The single-crystal structure of **MOC-35** (Fig. 1b and Tables S2 in Supporting information) unambiguously revealed an octahedral $Pd_6L_8$ cage consisted of eight ligands and six $Pd^{2+}$ ions, where the square-planar coordination of Pd-center is accomplished by four Pd-N bonds. The triphenylamine skeleton in L maintains the torsional $C_3$-symmetry, while pyridine moieties are twisted from planarity to wrap around the Pd-vertices (Fig. 1b). The distance along the diagonal of **MOC-35** is measured to be 26 Å, in consistence with above DOSY estimation.

It is a surprise that with the same feeding ratio of Pd/L = 3/4 by using $Pd(NO_3)_2$ instead of $[Pd(CH_3CN)_4](BF_4)_2$, a new cage structure was assembled (**MOC-36**) under similar conditions (Scheme 1), which exhibits distinct and complicated NMR signal profiles as compared with **MOC-34** and **MOC-35** (Figs. S1 and S14–S16 in Supporting information). The careful analyses of the $^1$H-$^1$H COSY and $^1$H-$^{13}$C HSQC spectra suggest that the $C_3$-symmetry of L ligands in this cage is seriously distorted, and three sets of proton signals are well resolved (Figs. S15 and S16), indicating a much lower symmetry of **MOC-36** than the octahedral **MOC-35**. The $^1$H DOSY spectrum of **MOC-36** (Fig. S17 in Supporting information) confirms that all proton signals have the same diffusion coefficient ($\log D = -10.17$), giving a dynamic radius of the cage at approximate 16.1 Å, which means **MOC-36** has a larger cage size than **MOC-35** (32 *vs.* 26 Å). The ESI-HR-MS spectrum shows a series of sharp peaks (Fig. S18 in Supporting information), exactly corresponding to the charge states of a $Pd_9L_{12}$ type cage varying from +10 to +5, namely, $[(Pd_9L_{12})^{18+}+nNO_3]^{(18-n)+}$ species which show perfect matching of the experimental and simulated isotopic patterns.

Unfortunately, we failed to grow its single-crystals suitable for X-ray diffraction although many efforts have been devoted. Therefore, optimization of the cage structure based on energy minimization was carried out, yielding a best fit cage model of tricapped trigonal prismatic geometry (Fig. 1c and Fig. S19 in Supporting information). Six Pd-centers constitute the vertices of a trigonal prism, the rest three Pd-centers serve as the side capping vertices, and twelve tridentate ligands occupy the lateral triangular faces. From the top view, **MOC-36** shows a general reuleaux triangle shape of $C_3$-symmetry; therefore, the size of **MOC-36** can be estimated as 32 × 23 Å when viewed along or perpendicular to the $C_3$-axis (Fig. S19), in good agreement with the result calculated from the $^1$H DOSY spectrum.

To our knowledge, the unique cage geometry of **MOC-36** has not been seen before in coordination cages. When compared with **MOC-35**, the two cage geometries are related (Fig. S20 in Supporting information). **MOC-36** consists of three quadrangular pyramids formed by three rectangular sides of the trigonal prism with three capping vertices, which are connected to form the reuleaux triangle shape. Similarly, **MOC-35** has two quadrangular pyramids glued together face-to-face. The dihedral angles between the pyramids are different in the two cages, with **MOC-36** having a larger angle, leaving more space for anion interactions (Fig. S20). This geometric difference may be the reason for the anion-induced cage transformation (*vide infra*). The low symmetry of the trigonal prismatic **MOC-36** makes the three pyridyl arms of each L ligand distinct, distinguishable from the positions to bind to different Pd-vertices (Fig. 1c). This explains why three sets of proton signals are observed in the NMR spectra of **MOC-36** (Figs. S15 and S16).

The above experiments showed that the type of cage formed depends on the metal-ligand ratio, with Pd/L ratios of 1/2 and 3/4 leading to **MOC-34** and **MOC-35/36**, respectively. To explore cage interconversions, $Pd^{2+}$ salt, L ligand, and ethylenediamine (en) chelator were added to seize $Pd^{2+}$ from the cage (Scheme 1 and Figs. S21–S35 in Supporting information). Adding $Pd(CH_3CN)_4(BF_4)_2$ to a solution of **MOC-34-BF$_4$** resulted in a single product transformation to **MOC-35-BF$_4$**, while adding $Pd(NO_3)_2$ to a DMSO solution of **MOC-34-NO$_3$** led to quantitative conversion to **MOC-36-NO$_3$** (Figs. S21–S24). The reverse cage conversion from **MOC-35** or **MOC-36** to **MOC-34** was also observed when L ligand or en was added (Figs. S25–S35 in Supporting information). In such reversible transformation processes, excess $Pd^{2+}$ salt or L ligand had little influence on the directional cage conversions, but excess en chelator destroyed the cage to liberate free L ligand. These results suggest that the Pd-N coordination allows for dissociation and association of the L ligand, but the Pd-L exchange speed is slower than the NMR time scale.

Counter anions are crucial in regulating the assembly and transformation of cage structures to form supramolecular isomers **MOC-35** or **MOC-36**. To study the impact of mixed $BF_4^-$ and $NO_3^-$ anions on the transformation process, $Pd(NO_3)_2$ or $Pd(CH_3CN)_4(BF_4)_2$ was added to the DMSO solution of **MOC-34-BF$_4$** or **MOC-34-NO$_3$**, respectively. A dynamic mixture of **MOC-35** and **MOC-36** was observed using NMR analysis (Figs. S36 and S37 in Supporting information) [7,8]. In contrast, using only one type of anion leads to the formation of one product: $BF_4^-$ leads to **MOC-35** and $NO_3^-$ leads to **MOC-36**. Both cages remain stable at room temperature for an extended period (Figs. S38 and S39 in Supporting information), but at elevated temperatures, **MOC-36** transforms to **MOC-35**, and not the other way around. **MOC-36** remains unchanged below 333 K but slowly transforms to **MOC-35** above this temperature (Figs. S40–S48 in Supporting information). It takes 15 days for complete conversion to **MOC-35-NO$_3$** at 353 K (Fig. S44 in Supporting information). NMR analysis shows that the converted **MOC-35-NO$_3$** has a comparable cage size to the self-assembled **MOC-35-BF$_4$** (Fig. S49 in Supporting information), but a stronger host-$NO_3$ interaction based on the remarkably downfield shifts of $H_d$ in **MOC-35** (Fig. S50 in Supporting information), indicating dynamic host-anion interactions underneath the Pd-vertices. Heating accelerates the cage transformation, with a rate constant of $5.02 \times 10^{-10}$ mol $L^{-1}$ $s^{-1}$ at 353 K and an activation barrier of 123.9 kJ/mol. These experiments suggest that **MOC-36** is kinetically favored, while **MOC-35** is thermodynamically preferred.

The anion effect on the cage isomerization has been further studied by adding $[(n\text{-Bu})_4N]BF_4$ to **MOC-36** (Fig. S52 in Supporting information). Despite $BF_4^-$ having weaker binding affinity than $NO_3^-$, adding large excess of $BF_4^-$ leads to competition with $NO_3^-$ to dominate host-anion interactions, resulting in a significantly increased **MOC-36**-to-**MOC-35** conversion rate (Figs. S52–S61 in Supporting information). Adding 180 equiv. $BF_4^-$ leads to a complete **MOC-36**-to-**MOC-35** conversion in 72 h at 353 K (Fig. 2a), over five times faster than the conversion without $BF_4^-$ anions. At a higher temperature, the conversion is even more rapid, taking only 10 h at 373 K (Fig. 2b and Fig. S58 in Supporting information). The conversion rate at 353 K is calculated to be $k = 2.87 \times 10^{-9}$ mol $L^{-1}$ $s^{-1}$, over five times faster than the rate without $BF_4^-$ anions. The conversion activation barrier for **MOC-36** is significantly lower at 106.6 kJ/mol under 180 equiv. $BF_4^-$ condition (Fig. S61 in Supporting information), indicating a significant role of host-anion dynamic interactions in altering the energy barrier for **MOC-36**-to-**MOC-35** structural transformation with $BF_4^-$ anions. However, a reversible **MOC-35**-to-**MOC-36** cage conversion is difficult to achieve, no matter by heating (Fig. S39) or adding excess $NO_3^-$ anions (Fig. S51).

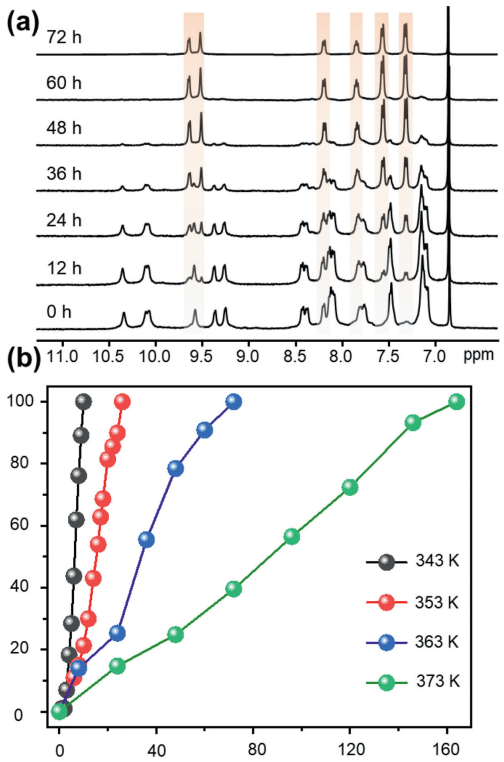


**Fig. 2.** (a) The progress of cage conversion from **MOC-36** to **MOC-35** at 353 K in 72 h after addition of 180 equiv. $(n\text{-Bu})_4NBF_4$ by *in situ* $^1H$ NMR (400 MHz, 298 K, DMSO-$d_6$). (b) Time courses of the cage conversion at different temperatures in the presence of 180 equiv. $(n\text{-Bu})_4NBF_4$.

More information about host-anion interactions was provided by the single-crystal structural analyses of **MOC-35-NO$_3$** and **MOC-35-BF$_4$** (Figs. 3a and b). Six anions are bound inside pockets underneath the Pd-vertices, forming C-H···O or C-H···F hydrogen bonds with the host through the pyridyl and phenyl rings. Density functional theory (DFT) calculations for fragmental $NO_3$@$[Pd(Py\text{-}Ph)_4]^{2+}$ and $BF_4$@$[Pd(Py\text{-}Ph)_4]^{2+}$ (Py = pyridyl, Ph= phenyl) were carried out based on the single-crystal structures of **MOC-35-NO$_3$** and **MOC-35-BF$_4$**, respectively. The total binding energy per anion for **MOC-35-NO$_3$** is calculated to be −545.7 kJ/mol, while for **MOC-35-BF$_4$**, it is −583.8 kJ/mol. In **MOC-35**, the tetrahedral $BF_4^-$ shows better shape complementarity than the planar $NO_3^-$, although the latter has stronger individual hydrogen bonding. We also calculate the total binding energies per anion for $NO_3$@$[Pd(Py\text{-}Ph)_4]^{2+}$ or $BF_4$@$[Pd(Py\text{-}Ph)_4]^{2+}$ units based on the simulated structure of **MOC-36** (Figs. 3c and d), giving significantly different enthalpy values of −595.6 kJ/mol for **MOC-36-NO$_3$** and −551.2 kJ/mol for the postulated **MOC-36-BF$_4$**. It is apparent that the $NO_3^-$ binding is

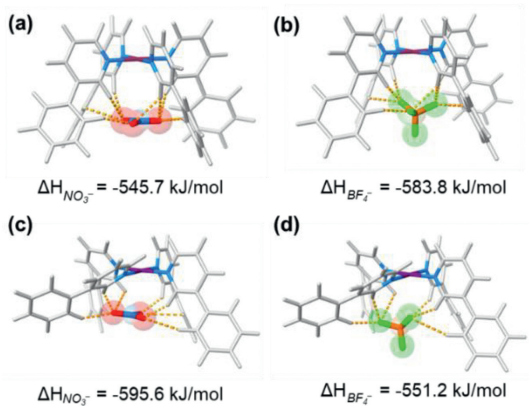


**Fig. 3.** (a, b) The total binding energies per anion calculated using DFT methods based on the crystal structures of **MOC-35-NO$_3$** and **MOC-35-BF$_4$**. (c, d) The total binding energies per anion calculated using DFT methods based on the energy-minimized cage model of **MOC-36**.

much more conducive to stabilize the Pd-vertices in **MOC-36** than the $BF_4^-$ binding, which adequately explains why the cage structure of **MOC-36** is easily generated in the presence of $NO_3^-$ anions.

The crystal structure analysis and theoretical calculations presented here support experimental observations of anion-induced cage self-assembly and transformation. The tetrahedral $BF_4^-$ fit best in **MOC-35**'s vertex pockets, while planar $NO_3^-$ fit best in **MOC-36**'s, forming strong host-anion interactions. This controls the stoichiometric cage transformation from **MOC-34** to **MOC-35** with $BF_4^-$ and **MOC-36** with $NO_3^-$. The Pd-N coordination is intrinsically dynamic, allowing for cage isomerization from kinetically favored **MOC-36** with tensive N-Pd-N dihedral angles to thermodynamically preferred **MOC-35** with relatively relaxed N-Pd-N dihedral angles. While **MOC-36** is stabilized at room temperature by $NO_3^-$, heating and adding a large excess of $BF_4^-$ can expedite cage isomerization *via* dynamic guest exchange. Ultimately, **MOC-35**, with better host-guest fitting to $BF_4^-$, will entirely replace the constitutional dynamic library of **MOC-35** and **MOC-36**.

The significant differences in cage size and windows of **MOC-35** and **MOC-36** could endow them with distinct guest inclusion behaviors [40]. To confirm this, we tested the inclusion of four different aromatic hydrocarbons including phenanthrene-9-carbaldehyde (**G1**), pyrene-1-carbaldehyde (**G2**), 4-(diphenylamino)benzaldehyde (**G3**) and 2,4,5-triphenyl-1*H*-imidazole (**G4**) with distinguishable molecular symmetry and aromatic moiety (Fig. 4a).

The study of guest encapsulation was performed in a DMSO-$d_6$/$D_2O$ = 2/1 (v/v) mixture (Figs. S62–S97 in Supporting information). For **MOC-35** (Figs. S62–S74), the proton signals of the host display remarkable shifts, of which the Py protons $H_a$ and $H_d$ generally move downfield while the Ph protons $H_e$ and $H_f$ move upfield (Fig. 4b and Fig. S74). All guest signals are up-field shifted, evidently due to a shielding effect of L center toward the encapsulated guests. The association constants corresponding to the interactions between the four guests and **MOC-35** cage were estimated by $^1$H NMR titrations (Fig. 4c) [41]. The relative strong host-guest interacitons with $K_a$ values in the 1279∼3893 L/mol range are determined. Formation of G⊂**MOC-35** clathrates *via* fast guest exchange has been further verified by $^1$H DOSY spectra, which disclose that the diffusion coefficients of the exchanging guests fall in between those of the free guests and the host, showing the weighted average of the coefficients of the free and bound guests [42].

For comparison, **MOC-36** has a even larger cavity and open windows, so the guest molecules can undergo much faster guest exchange *via* the cage windows, thus display weaker binding behavoir with the host. This expection is well supported by the $^1$H NMR and $^1$H DOSY measurements (Figs. S75–S87). Upon guest titrations, the protons of the host appear to be less affected, while those of guest molecules show slight chemical shift changes (Fig. 4b). The binding constants of aforementioned guests are determined similarly using Bindfit method (Fig. 4c). The relatively smaller $K_a$ values in the 656∼1141 L/mol range indicate even fast exchange behavior of the guests and their weaker binding ability towards **MOC-36** than **MOC-35**, which are further confirmed by the $^1$H DOSY data with closer diffusion coefficients of the exchanging guests to those of the free guest (Fig. 4c). Such different guest binding behaviors suggest a potential to tune the cage cavities *via* supramolecular isomerization to meet the demand of separation, catalysis and sensing for varied guests with appreciate kinetics and thermodynamics. It is noteworthy that the cage **MOC-34** with small cavity but large windows shows more similar guest encapsulation behavior with **MOC-36** than **MOC-35**, evidented by the relatively small proton signal changes and larger difference in $^1$H DOSY spectra (Figs. S89–S97).

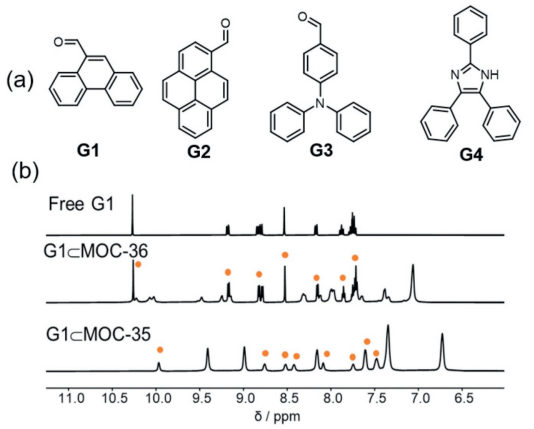


(c)

| | Binding constant $K_a$ (L/mol) | | Guests' diffusion coefficient (log*D*) | | |
|---|---|---|---|---|---|
| | MOC-35 | MOC-36 | $G_{free}$ | G⊂MOC-35 | G⊂MOC-36 |
| **G1** | 3893 | 487 | -9.22 | -9.52 | -9.28 |
| **G2** | 1560 | 1141 | -9.28 | -9.63 | -9.48 |
| **G3** | 2255 | 870 | -9.37 | -10.05 | -9.95 |
| **G4** | 1279 | 656 | -9.45 | -10.10 | -9.92 |

**Fig. 4.** (a) Four aromatic hydrocarbons (G1-G4) used for the guest binding study. (b) $^1$H NMR comparison of guest G1 inclusion by **MOC-35** and **MOC-36** in the solvent mixture of DMSO-$d_6$ and $D_2O$ (2:1, v/v). (c) Corresponding binding constants ($K_a$) and guest diffusion coefficients (log*D*).

In summary, we have described self-assembly of three different types of Pd-based metal-organic cages, **MOC-34**, **MOC-35**, and **MOC-36**. The stoichiometric cage transformations from $Pd_2L_4$-type **MOC-34** to $Pd_6L_8$-type **MOC-35** or unprecedented $Pd_9L_{12}$-type **MOC-36** are well-controlled by anion template induction, while the cage isomerization from **MOC-36** to **MOC-35** is found to be thermal-driven and significantly affected by dynamic host anion interactions. The experimental and calculation results reveal diversified influence of anion effect to trigger and control kinetics and thermodynamics in cage assembly and conversion processes. The distinguishable guest binding behaviors by virtue of supramolecular cage isomerization have been investigated. This study provides an example that helps to understand the interplay between anion templates and host-anion dynamics in the artificial mimicry of natural anion receptors, which is crucial for the self-assembly and transformation of cage hosts.

## Declaration of competing interest

The authors declare that they have no known competing financial interests or personal relationships that could have appeared to influence the work reported in this paper.

## Acknowledgments

This work was supported by the NKRD Program of China (No. 2021YFA1500401), the National Natural Science Foundation of China (Nos. 21821003, 21890380), and the LIRTP of Guangdong Pearl River Talents Program (No. 2017BT01C161).

## Supplementary materials

Supplementary material associated with this article can be found, in the online version, at doi:10.1016/j.cclet.2023.108477.

## References

[1] C.M. Dobson, A. Šali, M. Karplus, Angew. Chem. Int. Ed. 37 (1998) 868–893.
[2] D. Fujita, Y. Ueda, S. Sato, et al., Nature 540 (2016) 563–566.
[3] X.Q. Guo, L.P. Zhou, S.J. Hu, et al., J. Am. Chem. Soc. 143 (2021) 6202–6210.
[4] H. Wang, C. Guo, X. Li, CCS Chem. 4 (2022) 785–808.
[5] Y. Gong, Y. Zhang, C. Qin, et al., Angew. Chem. Int. Ed. 58 (2019) 780–784.
[6] M. Fujita, K. Umemoto, M. Yoshizawa, et al., Chem. Commun. (2001) 509–518.
[7] P.T. Corbett, J. Leclaire, L. Vial, et al., Chem. Rev. 106 (2006) 3652–3711.
[8] Z. Yang, J.M. Lehn, J. Am. Chem. Soc. 142 (2020) 15137–15145.
[9] Y.L. Ding, C.S. Shen, F.W. Gan, et al., Chin. Chem. Lett. 32 (2021) 3988–3992.
[10] L.X. Cai, D.N. Yan, P.M. Cheng, et al., J. Am. Chem. Soc. 143 (2021) 2016–2024.
[11] P.M. Cheng, L.X. Cai, S.C. Li, et al., Angew. Chem. Int. Ed. 59 (2020) 23569–23573 .
[12] S. Bandi, A.K. Pal, G.S. Hanan, D.K. Chand, Chem. Eur. J. 20 (2014) 13122–13126.
[13] T. Wu, Z. Jiang, X. Xue, et al., Chin. Chem. Lett. 32 (2021) 1911–1914.
[14] K. Li, K. Wu, Y.Z. Fan, et al., Natl. Sci. Rev. 9 (2021) nwab155.
[15] L. Liang, W. Zhao, X.J. Yang, B. Wu, Acc. Chem. Res. 55 (2022) 3218–3229.
[16] H. Zhang, Y. Li, Y.F. Zhang, et al., Chem. Eur. J. 29 (2023) e202300209.
[17] E. Benchimol, B.N.T. Nguyen, T.K. Ronson, J.R. Nitschke, Chem. Soc. Rev. 51 (2022) 5101–5135.
[18] K. Su, S. Du, W. Wang, D. Yuan, Chin. Chem. Lett. 31 (2020) 2023–2026.
[19] W.J. Shi, X. Li, P. Li, Y.F. Han, Nano Res. 15 (2022) 2655–2660.
[20] B. Moulton, M.J. Zaworotko, Chem. Rev. 101 (2001) 1629–1658.
[21] B. Wang, Z. Zang, H. Wang, et al., Angew. Chem. Int. Ed. 52 (2013) 3756–3759.
[22] B. Hasenknopf, J.M. Lehn, N. Boumediene, et al., Angew. Chem. Int. Ed. 37 (1998) 3265–3268.
[23] Y. Liu, W. Zhao, C.H. Chen, A.H. Flood, Science 365 (2019) 159–161.
[24] H. Duan, F. Cao, M. Zhang, et al., Chin. Chem. Lett. 33 (2022) 2459–2463.
[25] X. Kan, H. Liu, Q. Pan, et al., Chin. Chem. Lett. 29 (2018) 261–266.
[26] R. Sekiya, M. Fukuda, R. Kuroda, J. Am. Chem. Soc. 134 (2012) 10987–10997.
[27] I.A. Riddell, M.M.J. Smulders, J.K. Clegg, et al., Nat. Chem. 4 (2012) 751–756.
[28] W.M. Bloch, J.J. Holstein, B. Dittrich, et al., Angew. Chem. Int. Ed. 57 (2018) 5534–5538.
[29] S. Mecozzi, J. Rebek, Chem. Eur. J. 4 (1998) 1016–1022.
[30] R. Custelcean, Chem. Soc. Rev. 43 (2014) 1813–1824.
[31] Y. Chen, J.W.Y. Lam, R.T.K. Kwok, et al., Mater. Horiz. 6 (2019) 428–433.
[32] S.P. Zheng, L.B. Huang, Z. Sun, M. Barboiu, Angew. Chem. Int. Ed. 60 (2021) 566–597.
[33] D.E. Koshland Jr., Angew. Chem. Int. Ed. 33 (1995) 2375–2378.
[34] C.Y. SU, A.M. Goforth, M.D. Smith, H.C. ZurLoye, Inorg. Chem. 42 (2003) 5685–5692.
[35] J.J. Jiang, J.R. He, X.Q. Lu, et al., IUCrJ 1 (2014) 318–327.
[36] M. Pan, K. Wu, J.H. Zhang, C.Y. Su, Coord. Chem. Rev. 378 (2019) 333–349.
[37] D.X. Cui, Y. Geng, J.N. Kou, et al., Nat. Commun. 13 (2022) 4011.
[38] L.L. Ma, Y.Y. An, L.Y. Sun, et al., Angew. Chem. Int. Ed. 58 (2019) 3986–3991.
[39] Y.S. Wang, L.Y. Sun, Y.Y. Wang, Y.F. Han, Sci. China Chem. 65 (2022) 1129–1133.
[40] L.J. Wang, S. Bai, Y.F. Han, J. Am. Chem. Soc. 144 (2022) 16191–16198.
[41] P. Thordarson, Chem. Soc. Rev. 40 (2011) 1305–1323.
[42] L. Fielding, Prog. Nucl. Magn. Reson. Spectrosc. 51 (2007) 219–242.